remote sensing

MDPI

Article

Statistical Characteristics of the Multiscale SST Fractal Structure over the Kuroshio Extension Region Using VIIRS Data

Kai Yu [1,2,3,*], Changming Dong [4], Jin Wang [4], Xuhua Cheng [1,3] and Yi Yu [2]

[1] Key Laboratory of Marine Hazards Forecasting, Ministry of Natural Resources, Hohai University, Nanjing 210024, China
[2] State Key Laboratory of Satellite Ocean Environment Dynamics, Second Institute of Oceanography, Ministry of Natural Resources, Hangzhou 310005, China
[3] College of Oceanography, Hohai University, Nanjing 210024, China
[4] School of Marine Sciences, Nanjing University of Information Science and Technology, Nanjing 210044, China
* Correspondence: yukai041@hhu.edu.cn; Tel.: +86-13-915-925-964

Abstract: The ocean behaves as a typical multiscale fractal structure, whose dynamic and thermal variabilities extend over a wide range of spatial scales, r, spanning from 10^{-3} to 10^{7} m. Studying the statistical characteristics of multiscale fractal structures is crucial to understanding the interactions and energy cascade processes between different spatial scales. Remote sensing data are one of the best choices for revealing these statistical characteristics. This work analyzes the multiscale (1–1000 km) fractal structures of sea surface temperature (SST) from the Level-2+ (L2P) satellite orbit Visible Infrared Imaging Radiometer Suite (VIIRS) products over the Kuroshio Extension (KE) region (145°E–160°W, 20°N–50°N), using a conventional method (second-order structure function, $D(r)$) and a newly developed statistical method (spatial variance, $V(r)$). The results show that both the power-law distribution slopes of $D(r)$ and $V(r)$ are close to 2/3, which is equivalent to the $-5/3$ wavenumber spectrum. $V(r)$ is found to be more robust when depicting the fractal structure and variance density, $V'(r)$, compared with $D(r)$. $V'(r)$ is slightly larger at the mesoscale (50–150 km) than at the large scale (higher than 150 km) and is much smaller than that at the submesoscale (smaller than 50 km). Additionally, $V'(r)$ has an indiscernible diurnal variation but remarkable seasonal and latitudinal variations. For the seasonal variability, the maximum $V'(r)$ appears in winter at the large scale and mesoscale, and gradually shifts towards spring at the submesoscale, which implies that a forward energy cascade process may occur during this period. The maximum of the latitude-dependent $V'(r)$ appears around 40°N for all the scales. It is consistent with the latitude of the strongest background SST gradient, indicating that the background SST front is the main source of the strong SST multiscale spatial variabilities over the KE region. This work benefits the application of other high-resolution remote sensing data in this research field, including the forthcoming Surface Water Ocean Topography (SWOT) satellite product.

Keywords: submesoscale; energy cascade; structure function; spatial variance; sea surface temperature; Kuroshio Extension

check for updates

Citation: Yu, K.; Dong, C.; Wang, J.; Cheng, X.; Yu, Y. Statistical Characteristics of the Multiscale SST Fractal Structure over the Kuroshio Extension Region Using VIIRS Data. *Remote Sens.* **2023**, *15*, 881. https://doi.org/10.3390/rs15040881

Academic Editor: Enric Valor

Received: 23 November 2022
Revised: 27 January 2023
Accepted: 2 February 2023
Published: 5 February 2023

Copyright: © 2023 by the authors. Licensee MDPI, Basel, Switzerland. This article is an open access article distributed under the terms and conditions of the Creative Commons Attribution (CC BY) license (https://creativecommons.org/licenses/by/4.0/).

1. Introduction

Ocean motions have multiscale fractal structure characteristics, which can be roughly divided into large-scale circulations, mesoscale eddies, submesoscale processes, and microscale turbulence. Kolmogorov [1] revealed a kinetic energy spectrum of $\psi(k) \sim k^{-5/3}$ (where k is the wave number) for the inertial range of three-dimensional (3-D) homogeneous isotropic turbulence through dimensional analysis. A forward energy cascade (large structures of motion break down into smaller structures in a chain process) occurs in the inertial range. This theory is considered as one of the bases for classical microturbulence theory. As

the large-scale motions of the atmosphere and ocean are closer to quasi-two-dimensional, Kraichnan [2] derived a new statistical law to describe the barotropic two-dimensional (2-D) turbulence characteristics. Two-dimensional turbulence exhibits two inertial ranges: an inverse kinetic energy cascade with a kinetic energy spectrum of $\psi(k) \sim k^{5/3}$ at larger scales and a forward enstrophy cascade with a spectrum of $\psi(k) \sim k^{-3}$ at smaller scales. More theories were subsequently introduced to depict the spectral behaviors of atmospheric and oceanic multiscale fractal structures.

The quasi-geostrophic (QG) theory is a cornerstone for the study of ocean flow. The QG flow can be caused by the interior PV anomalies and surface buoyancy anomalies. Charney [3] considered the QG flows component due to interior PV anomalies that are far enough from surface buoyancy. He argued that there is a forward energy cascade of the potential enstrophy in the submesoscale inertial range, and the power-law behaviors of the kinetic energy and available potential energy wavenumber spectrum show a slope of -3. The applicable region of Charney's theory is far from the surface. As a supplement, Blumen [4] considered the flow associated with surface buoyancy anomalies with a uniform interior PV. His theory is often referred to as the surface QG theory. It predicted a potential energy wavenumber spectrum with a slope of $-5/3$. Klein et al. [5] reported a wavenumber spectrum slope of -2 for both active and passive tracers in response to frontogenesis.

According to these theories, various observations were used to statistically demonstrate the spectral behaviors of atmospheric and oceanic multiscale fractal structures, such as sounding balloons, commercial aircraft, and remote sensing satellites [6–8] in the atmospheric science field, and satellite altimetry, Acoustic Doppler Current Profiler (ADCP) data, and Argo profiling floats [9–11] in the oceanic science field. These observations help to provide a global view of atmospheric and oceanic motions, which can advance our understanding of interactions among different scales. However, the systematic oceanic multiscale fractal structure, from submesoscale to large scale (0–1~1000 km), is still poorly understood, especially for the submesoscale range, which is mainly limited by the resolution of the observational data. As for now, remote sensing data are one of the best choices in the statistical study of sea surface multiscale fractal structures due to their large coverage, abundant sampling, and high resolution. Among various remote sensing variables, the sea surface temperature (SST) measurement was developed relatively early and is thus mature and has higher accuracy.

This work uses the Level-2+ (L2P) Visible Infrared Imaging Radiometer Suite (VIIRS) remote sensing SST data in satellite swath coordinates [12] to statistically identify the oceanic multiscale fractal structure. As a new generation of radiometer, VIIRS has a wider swath (~3040 km), higher spatial resolutions (~750 m at nadir for the M-bands), and more spectral bands (22 spectral bands), providing global daily coverage for both day and night passes [13]. Compared with the gridded Level-3 (L3) and Level-4 (L4) satellite products, the noninterpolated L2P products reserve higher spatiotemporal resolution and synchronization.

The main traditional method to obtain the power-law behaviors of the turbulence fractal structure is the spectral approach. It is based on Fourier transform, requiring the data to be regular, straight, and gap-free. This method usually uses buoy observations and numerical model data to describe the oceanic mesoscale and submesoscale turbulence structures [14–19]. The spectral approach is unavailable for the patchy L2P VIIRS data with cloud and rainfall cover. Another traditional method, the second-order structure function, which has a high tolerance for missing data, can solve this problem. In addition, Vogelzang et al. [20] developed a new statistical method named the spatial variance method. It can measure the exact variance density at a particular scale band (similar to the spectral techniques) and has a high tolerance for missing data [21].

The Kuroshio Current carries enormous heat and momentum northwards, and deflects eastward to form the Kuroshio Extension (KE) around 35°N after reaching Japan. The KE region has a strong ocean front [22] and energetic multiscale motions both in the

atmosphere [23] and ocean [24–26]. Therefore, the region is an ideal experimental zone to study the multiscale fractal structure.

This work combines the structure function and spatial variance method to analyze the statistical characteristics of the multiscale fractal structure over the KE region with L2P SST data observed by VIIRS. Section 2 introduces the data used in the study. Section 3 describes the structure function and spatial variance method, and the method validation. The main results, including mean state and spatiotemporal variability of the statistical characteristics of the multiscale fractal structure, are presented in Section 4. The results are summarized and discussed in Section 5.

2. Data

2.1. VIIRS L2P SST

The Suomi National Polar-orbiting Partnership (S-NPP) satellite launched on 28 October 2011 to fly in a circular near-polar orbit located at an altitude of 824 km above the Earth, with an inclination angle of 98.79° to the equator. The L2P SST product used in this work is observed by the VIIRS onboard S-NPP. It is provided by the Group for High-Resolution Sea Surface Temperature (GHRSST) and the Office of Satellite and Product Operations (OSPO) of the National Oceanic and Atmospheric Administration (NOAA). The VIIRS SST product is derived using the NOAA's Advanced Clear-Sky Processor for Ocean (ACSPO) system by retrieving four brightness temperatures in the M12 (3.7 μm), M14 (8.6 μm), M15 (11 μm), and M16 (12 μm) bands.

Figure 1 shows an example of VIIRS L2P SST data on 14 March 2015 over the KE region. Abundant submesoscale structures (with spatial scale smaller than 50 km) are clearly discernable in this plot. Meanwhile, there are substantial missing points due to cloud coverage. VIIRS provides a cloud classification for each pixel: clear, probably clear, or cloudy. Here, we estimate the effective data ratio by calculating the ratio between the number of pixels for clear and probably clear weather conditions to the total number of pixels (Figure 2). The effective data ratio is only around 18% for clear weather and ~23% for probably clear. Both of them are higher in summer (JJA) and fall (SON) than in winter (DJF) and spring (MAM). Considering the computation load, only the data during 2015 are used in the present work.

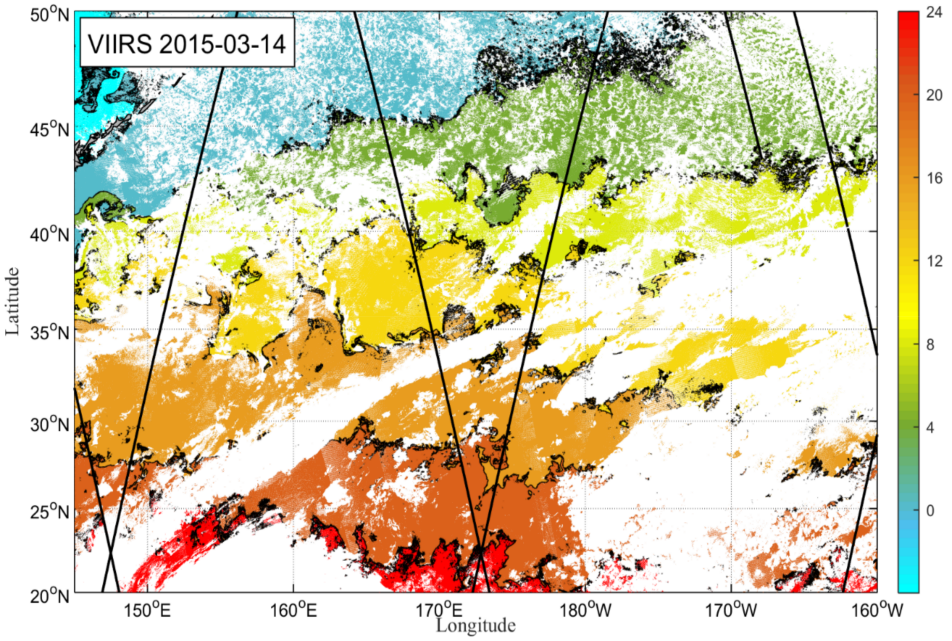

Figure 1. SST image composited by all the available VIIRS L2P data on 14 March 2015 over the KE region (145°E–160°W, 20°N–50°N). The background color denotes SST (°C) and the black straight lines show the nadir orbital paths of the satellites.

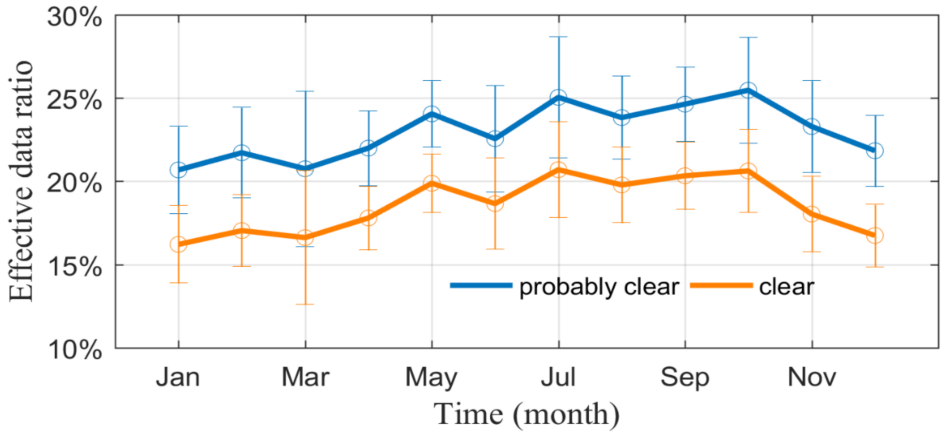

Figure 2. Monthly effective data ratio during 2015 over the KE region for clear (orange) and probably clear (blue) weather conditions. The error bars are the standard deviation of the mean.

The VIIRS instrument is a whiskbroom scanning radiometer (Figure 3a), with a scan length of ~3040 km along the cross-track direction, which is equivalent to the swath width. A total of 16 detectors produce 16 rows of pixels for each scan. The constant angular resolution of the detectors results in an increased pixel size further from the nadir. Thus, the resolution is finer (~0.75 km) at the nadir, and there is no overlap between adjacent scans (Figure 3b), while the resolution is coarser (~1.5 km) at the swath edge and the scans overlap (Figure 3c). These characteristics decide the samples' selection when calculating the spatial variance and structure function below.

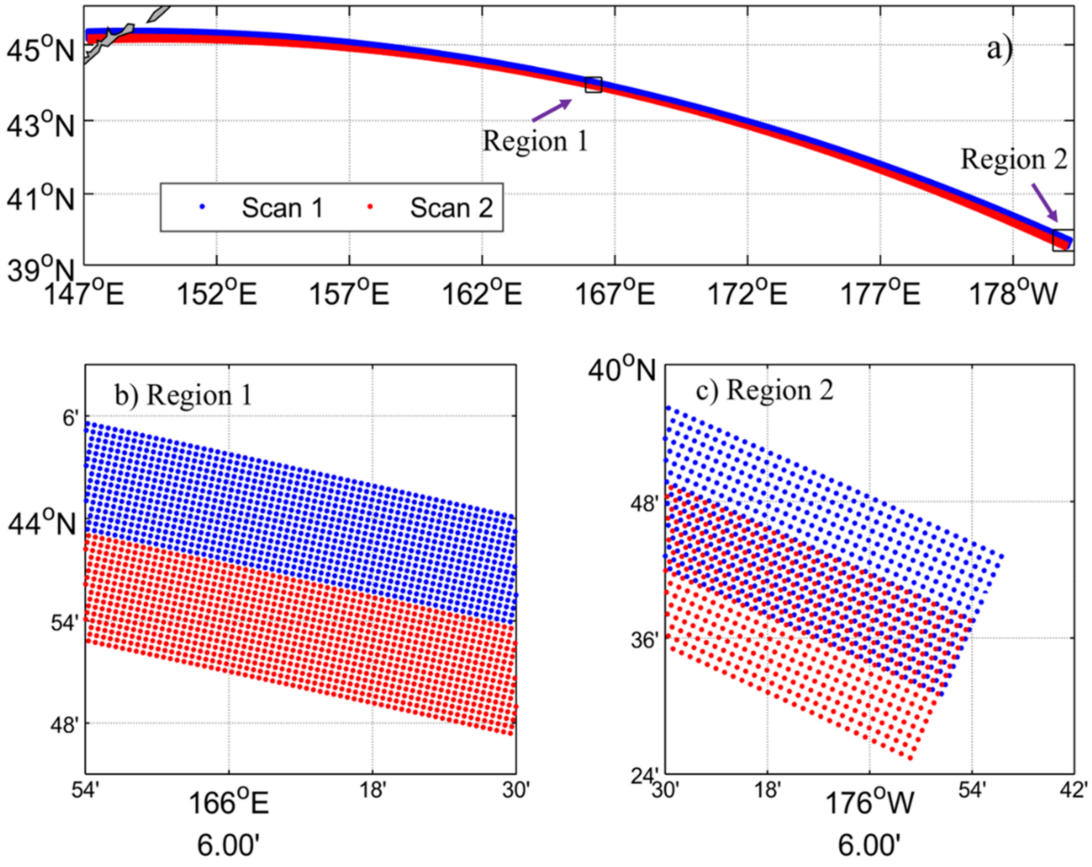

Figure 3. (**a**) Example of adjacent two scans of the VIIRS. (**b**,**c**) are two enlarged figures, respectively, for Region 1 (at nadir) and Region 2 (edge-of-scan) in (**a**).

2.2. GHRSST L4 SST

GHRSST L4 product in 2015 is used to describe the background SST front. The daily GHRSST L4 product is produced by the UK Met Office on a global 0.054° grid. It is generated from the analysis of multiple sources of lower-level satellite data using optimal interpolation.

3. Methods

3.1. Spectral Approach and Second-Order Structure Function

Two traditional methods to estimate the power-law behavior of the multiscale fractal structure of turbulent kinetic energy (TKE) or tracer variance are spectral analysis and second-order structure functions. The spectral approach can obtain the so-called wavenumber spectrum, $\psi(k) \sim k^{\beta}$, with the spectral slope of β through the Fourier transform. $\psi(k)$ stands for the variance density at different wavenumbers. The Fourier transform requires the samples without missing points. Although there are techniques to perform spectral decompositions with missing data, it is still challenging to do this with patchy data such as the L2P VIIRS data. For this reason, statistical studies of multiscale fractal structure, especially at the submesoscale, are commonly limited to data with high continuity, such as numerical model data and buoy observation.

On the other hand, the second-order structure function, $D(r)$, can help to solve this challenge. It is defined as $D(r) = E\left[(\delta\theta)^2\right]$, which can measure the scale-dependent TKE or tracer variance, where r is the spatial scale, θ is the variable (could be velocity, potential temperature, salinity or other generic tracers), $\delta\theta = \theta(x, r) - \theta(x)$ stands for the variable increment between the pair of points $x + r$ and x, and E denotes the expectation operator.

If the spectrum has a power-law behavior of $\psi(k) \sim k^{\beta}$, a related power-law $D(r) \sim r^{p}$ is expected for the second-order structure function. According to Webb [27], they obey

$$p = -\beta - 1 \tag{1}$$

Thus, for the classical $\psi(k) \sim k^{-5/3}$ Kolmogorov spectrum, $\beta = -5/3$ and $p = 2/3$.

3.2. Spatial Variance Method

According to Vogelzang et al. [20], $D(r)$ only measures the approximate scale-dependent variance of the variable. To obtain a more reliable measure of the variance, they developed the spatial variance method.

The spatial variance, $V(r)$, is defined as the expectation of sample variances $S^2(r)$ as a function of r

$$V(r) = E\left[S^2(r)\right] \tag{2}$$

where $S^2(r) = \frac{1}{r}\int_0^r [\theta(s) - \overline{\theta}(r)]\,ds$, and the sample average $\overline{\theta}(r) = \frac{1}{r}\int_0^r \theta(s)ds$.

For the point of numerical calculation, Vogelzang et al. [20] calculated $V(r)$ by

$$V(r) = E\left[M_2(r) - M_1^2(r)\right] \tag{3}$$

The first moment, $M_1(r)$, is equal to $\overline{\theta}(r)$, and the second moment $M_2(r) = \frac{1}{r}\int_0^r \theta^2(s)ds$.

According to its definition, $V(r)$ measures the cumulative variance over all the spatial scales smaller than r. Thus, the variance within a particular spatial scale range can be measured by

$$\Delta V(r_1, r_2) = V(r_2) - V(r_1) \tag{4}$$

Correspondingly, one can obtain the spatial variance density

$$V'(r) = \frac{d}{dr}V(r) \tag{5}$$

According to Vogelzang et al. [20], the correlation between the $V(r)$ and $D(r)$ is

$$V(r) = \frac{1}{r^2}\int_0^r (r-s)D(s)ds \tag{6}$$

When $D(r)$ follows a power-law, $D(r) = Cr^p$, with C a constant, substitution into Equation (6) yields

$$V(r) = \frac{Cr^p}{(p+1)(p+2)} \tag{7}$$

which leads to

$$\frac{V(r)}{D(r)} = \frac{1}{(p+1)(p+2)} \tag{8}$$

3.3. Method Framework

The VIIRS L2P SST data are a 2-D swath data. However, in this work, only the one-dimensional (1-D) spatial series along the cross-track direction are used to calculate $D(r)$ and $V(r)$. The reasons are as follows. Firstly, as shown in Figure 3c, the observation points are overlapped in the along-track direction at the swath edge. Although there is no overlap at the nadir, the pixel points in the along-track direction are not in a straight line (Figure 2b). That makes it difficult to calculate $D(r)$ and $V(r)$. Secondly, from the perspective of time synchronization, selecting the spatial series in the cross-track direction is better than that in the along-track direction because the cross-track series belong to the same scan.

Suppose we have a 1-D spatial series θ_i, $i = 1, 2, \cdots, N$. For a given scale $r = n\Delta r$, where n is the number of intervals ($N > n$) and Δr is the data spatial resolution, all the samples with interval number of n are collected to form a data matrix that has size $m \times (n+1)$

$$\begin{bmatrix} \theta_1 & \theta_2 & \cdots & \theta_{n+1} \\ \theta_2 & \theta_3 & \cdots & \theta_{n+2} \\ \vdots & \vdots & \ddots & \vdots \\ \theta_m & \theta_{m+1} & \cdots & \theta_{m+n} \end{bmatrix} \tag{9}$$

where m is the sample number, and $N = m + n$. The sample of the matrix is continuously expanded if there are more 1-D spatial series. Then, the sample mean is

$$\overline{\theta}_i(r) = \frac{1}{n+1}\sum_{j=i}^{n+i}\theta_j \tag{10}$$

and the sample variance is

$$S_i^2(r) = \frac{1}{n}\sum_{j=i}^{n+i}\left(\theta_j - \overline{\theta}_i(r)\right)^2 \tag{11}$$

Finally, the second-order structure function is

$$D(r) = \frac{1}{m}\sum_{i=1}^{m}(\theta_{i+n} - \theta_i)^2 \tag{12}$$

and the spatial variance is

$$V(r) = \frac{1}{m}\sum_{i=1}^{m} S_i^2(r) \tag{13}$$

It should be mentioned that this work uses the relatively intuitive method based on Equation (2) rather than Equation (3) to calculate $V(r)$. The results derived from these two equations are similar based on our calculation, and there is no obvious reduction in computation load when using Equation (3).

3.4. Fractional Brownian Motion Experiments

In order to validate the methods and equations mentioned in Sections 3.1 and 3.2, a nonstationary fractional Brownian motion (fBm) experiment was performed (Figure 4a). The 1-D spatial fBm series were set with a length of 3200 km and a resolution of 1 km to simulate the spatial series characteristics of the 1-D cross-track VIIRS data. The Hurst exponent (Hurst 1951) of the fBm series was set to $H = 1/3$ to simulate the spectrum of $\psi(k) \sim k^{-5/3}$. One thousand fBm series were stochastically generated to separately calculate $D(r)$, $V(r)$, and $\psi(k)$.

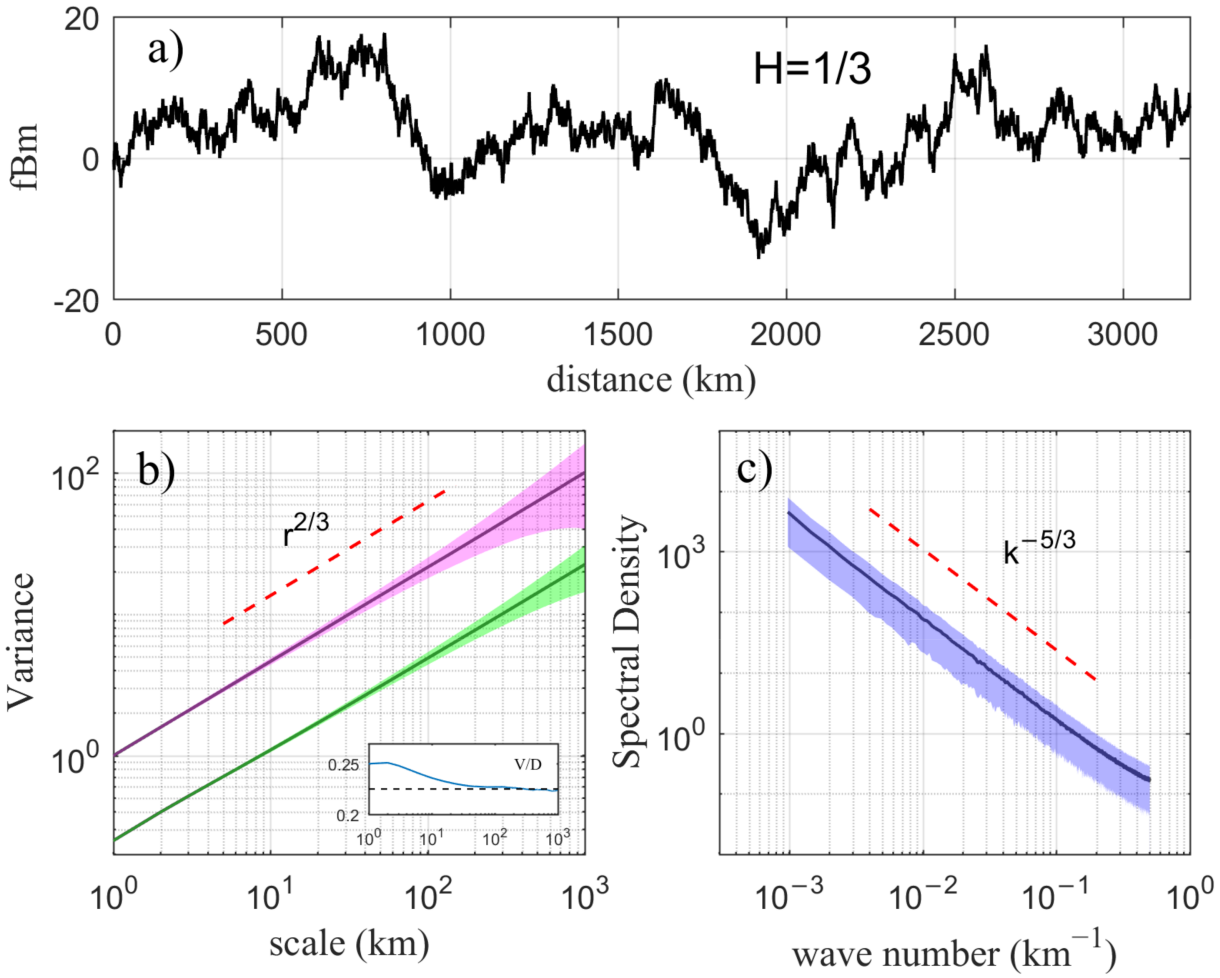

Figure 4. (**a**) Example of fBm series simulated with a Hurst exponent $H = 1/3$. Log–log plots of the mean (**b**) $D(r)$ (purple) and $V(r)$ (green) and (c) $\psi(k)$ (blue) derived from 1000 stochastically generated fBm series. Shadings indicate the standard deviations. Red dashed line in (**b**) indicates the $r^{2/3}$ power-law and in (**c**) indicates the $k^{-5/3}$ power-law. The subplot in (**b**) shows $\frac{V(r)}{D(r)}$, and the dashed line is the theoretical ratio predicted by Equation (8).

Figure 4b,c show that the mean $D(r)$, $V(r)$, and $\psi(k)$ obey the $r^{2/3}$ or $k^{-5/3}$ power-law, which satisfies Equation (1). The ratio between $V(r)$ and $D(r)$ is close to 0.25 at $r = 1$ km, and tends quickly to the theoretical ratio (0.23) predicted by Equation (8) as r increases. In addition, along with the increment of r, fewer samples can be achieved. Thus, one can see that the standard deviations of $D(r)$ and $V(r)$ obviously increase at larger scales (Figure 4b). However, the standard deviation of $V(r)$ is relatively smaller than that of $D(r)$, which is predictable because V makes use of all the points in one sample, while D only uses the two points at both ends. The high utilization ratio of the data is one advantage of the spatial variance method.

According to our estimation, nearly 75% of the L2P VIIRS SST data are missing over the KE region for probably clear weather conditions. In order to evaluate the tolerance for missing points, 75% of the 1-D fBm series used in the previous experiment are randomly flagged as missing before calculating $D(r)$ and $V(r)$. The new results are nearly the same as Figure 4b and thus are not shown. Therefore, both $D(r)$ and $V(r)$ have a high tolerance for missing points, and can be applied in this work.

4. Results

4.1. Power-Law of the Multiscale Fractal Structure

All of the available 1-D cross-swath VIIRS SST for probably clear weather over the KE region in 2015 were collected to build the data matrix in Equation (9) and calculate $D(r)$ and $V(r)$ for each day. Figure 5a shows the annual mean $D(r)$ and $V(r)$. Generally, $D(r)$ and $V(r)$ depict the same power-law distribution, which is close to $r^{2/3}$ ($k^{-5/3}$). The standard deviation of $D(r)$ is larger than that of $V(r)$ at scales larger than 100 km.

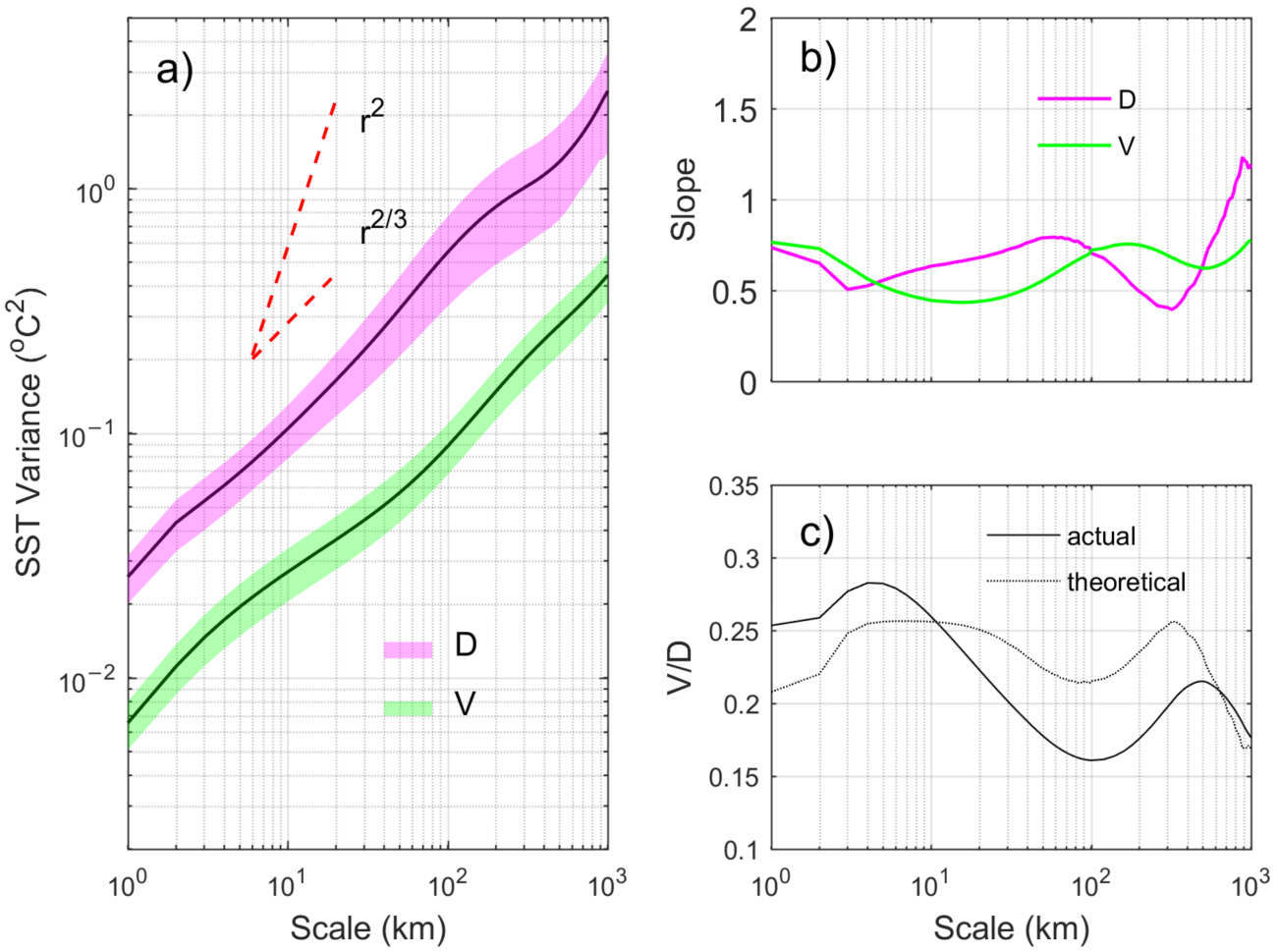

Figure 5. (**a**) Log–log plots of the mean $D(r)$ (purple) and $V(r)$ (green) derived from the VIIRS data (CI: °C^2). Shadings indicate the standard deviations. Red dashed lines indicate the $r^{2/3}$ and r^2 scaling law distribution. (**b**) Slopes of $D(r)$ and $V(r)$. (**c**) $\frac{V(r)}{D(r)}$ (solid line) and theoretical ratio (dashed line) predicted by Equation (8).

Figure 5b shows the slopes of $D(r)$ and $V(r)$ in Figure 5a. The slope are defined as $\frac{\mathrm{dlog}(D(r))}{\mathrm{dlog}(r)}$ and $\frac{\mathrm{dlog}(V(r))}{\mathrm{dlog}(r)}$, and are calculated by using a sliding three-point fit. We can see that the slopes vary from 0.5 to 1, and are close to 2/3. It is worth mentioning that the power-law of $r^{2/3}$ derived from the SST data cannot be explained by the 3-D turbulent kinetic energy spectrum of Kolmogorov [1]; instead, it should be interpreted as a potential

energy spectrum reported by the surface QG theory [4]. Due to the smaller amplitude of $V(r)$, its slope is more stable than that of $D(r)$. At the scales close to 1000 km, the slope for $D(r)$ even larger than 1. It indicates that $V(r)$ behaves better than $D(r)$ at larger scales, which is explained in the fBms experiments. Figure 5c shows that $\frac{V(r)}{D(r)}$ is 0.25 when $r = 1$ km, and decreases to ~0.2 at scale $r = 1000$ km. The theoretical ratio, which is calculated through Equation (8) by substituting the mean slope of $V(r)$ and $D(r)$, is well correlated with the actual value.

The slope of $V(r)$ shows obvious seasonal variabilities at different spatial scales (Figure 6). To better discuss the results, we roughly separate the spatial scales into large scale (larger than 150 km), mesoscale (50–150 km), and submesoscale (smaller than 50 km). At the large scale, the slope is larger in summer and smaller in other seasons. It is even as large as 1 at scales larger than 800 km. This steeper r^1 power-law is equivalent to the k^{-2} spectrum (Equation (1)). The seasonal variabilities of slope at the mesoscale and submesoscale are opposite to that for the large scale, showing a maximum in winter and minimum in summer. The maximum can also be close to 1 at around 150 km. Such a steeper k^{-2} spectrum is commonly reported at meso- and submesoscale [10,14,16], and is arguably influenced by the ageostrophic effects, which accelerate frontogenesis and frontal collapse [5,28].

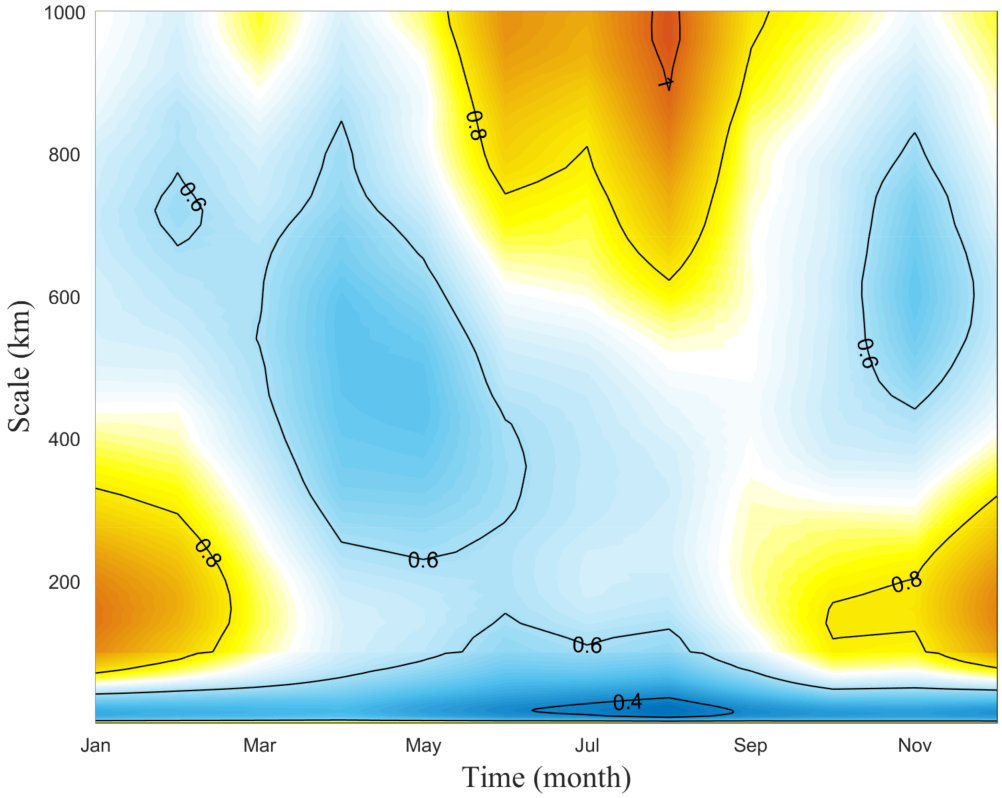

Figure 6. Scale–seasonal variability of the slope of $V(r)$ during 2015.

4.2. Spatial Variance Density

4.2.1. Mean State and Diurnal Variability

To analyze the energy density at different scales, we calculate the SST spatial variance density, $V'(r)$, based on Equation (5). As shown in Figure 7a, $V'(r)$ is invariant at scales larger than 400 km, which implies that energy is evenly distributed at these scales. $V'(r)$ gradually increases from 0.4×10^{-3} °C^2 km^{-1} at the large scale to 0.6×10^{-3} °C^2 km^{-1} at the mesoscale. As the spatial scale decreases, $V'(r)$ shows an exponential increment at the submesoscale. It can reach as high as 1.5×10^{-3} °C^2 km^{-1}, which is about three times larger than at other scales. It should be noted that the exponential increment of $V'(r)$

only happens at spatial scales smaller than 10 km. However, it is still unclear if the result is caused by the abundant high-frequency superinertial motions over this region [29] or simply from the observational noise.

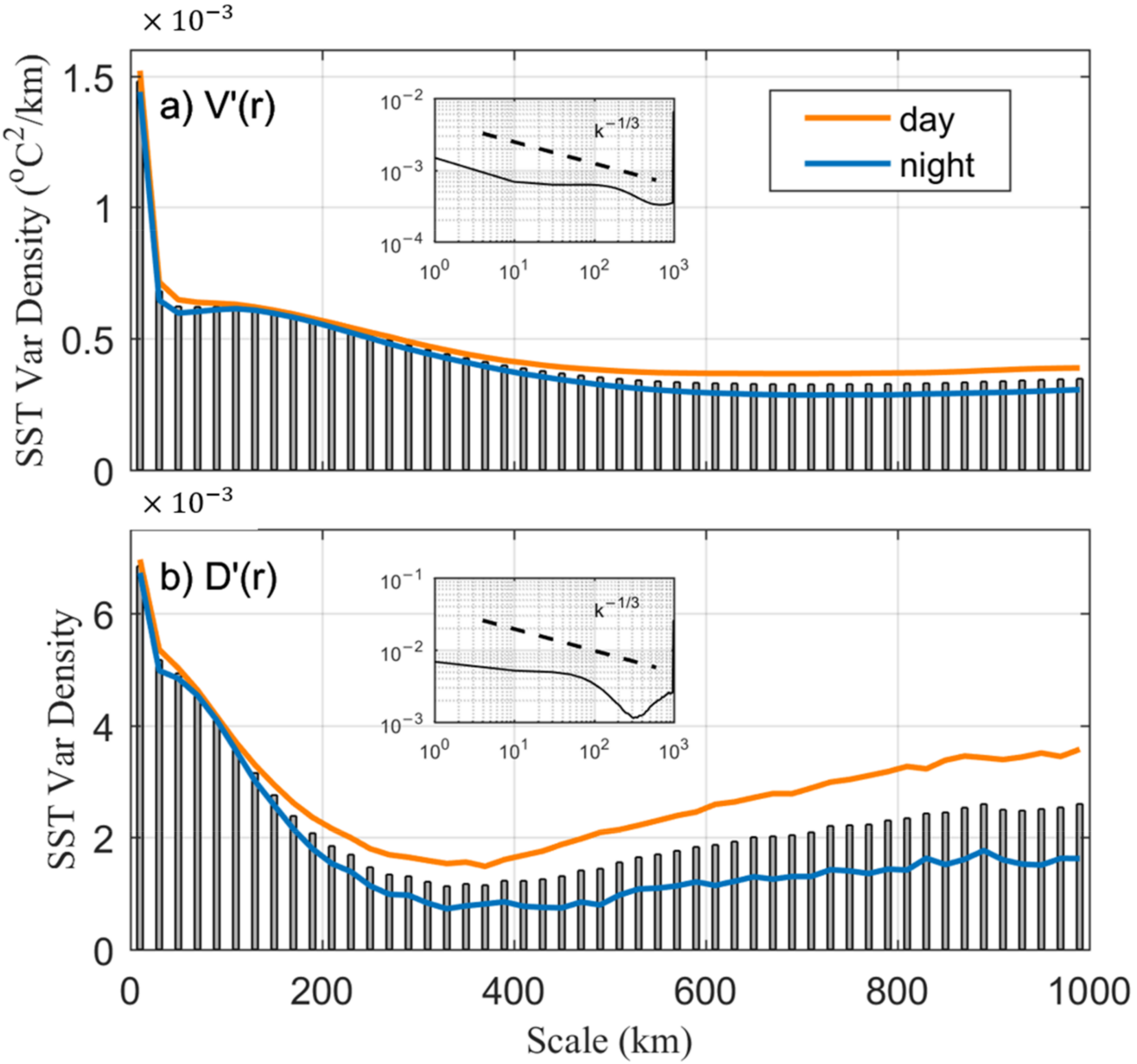

Figure 7. (**a**) Scale-dependent SST spatial variance density, $V'(r)$, and its diurnal variability. (**b**) is same as (**a**) but for the structure function results. The subgraphs in (**a**) and (**b**) shows the mean $V'(r)$ and $D'(r)$, which are similar to the main graphs but in logarithmic coordinates.

Figure 7a compares the differences in $V'(r)$ between daytime and nighttime. Generally, the difference is quite weak, which means there is ignorable diurnal variability of $V'(r)$. At the large scale, $V'(r)$ during daytime is slightly larger than during nighttime, which is because solar radiation can enhance the large-scale SST latitudinal gradient. In contrast, at the meso- and submesoscale, the diurnal variability is totally unrecognizable.

It is worth mentioning that the variance density is usually calculated by $D'(r) = \frac{d}{dr}D(r)$, similar to $V'(r)$ before the spatial variance method was developed. Figure 7b compares $V'(r)$ and $D'(r)$. Some obvious differences can be found between them. Firstly, $D'(r)$ is about four times larger than that of $V'(r)$. This ratio is consistent with that of

$\frac{D'(r)}{V'(r)} = \frac{D(r)}{V(r)} = (p+1)(p+2) \approx \frac{40}{9}$ according to Equation (8) in the ideal case of $p = 2/3$. Secondly, the change with scale for $D(r)$ is quite different from that of $V'(r)$. Thirdly, $D'(r)$ shows discernible diurnal variability, particularly at the large scale. At last, the $V'(r)$ and $D'(r)$ should obey the scaling law of $r^{-1/3}$ if $V(r) \sim r^{2/3}$ and $D(r) \sim r^{2/3}$. Figure 7a shows that the scaling law of $V'(r)$ fits well with $r^{-1/3}$, especially at the submesoscale and large scale. The slope at the mesoscale is relatively small. Conversely, $D'(r)$ does not fit very well with the scaling law of $r^{-1/3}$. These results demonstrate that the spatial variance method is more robust in depicting the scale-dependent variance density compared with the second-order structure function method.

4.2.2. Seasonal Variability

In the following study, only the spatial variance method is used due to its good performance in capturing the multiscale SST structure. Figure 8 exhibits the seasonal variability of $V'(r)$ at different scales. At the large scale, the maximum $V'(r)$ always occur in winter (Figure 8a–d), mainly due to the stronger background SST latitudinal gradient and wind stirring over the KE region during this season. The minimum $V'(r)$ occurs in November at the 800 km (Figure 8a) and 600 km (Figure 8b) scales, but in August at the 400 km (Figure 8c) and 200 km (Figure 8d) scales. For the meso- and submesoscale results (Figure 8e–g), the minimum occurs in August. Conversely, the maximum gradually switches from January to April as the scale decreases.

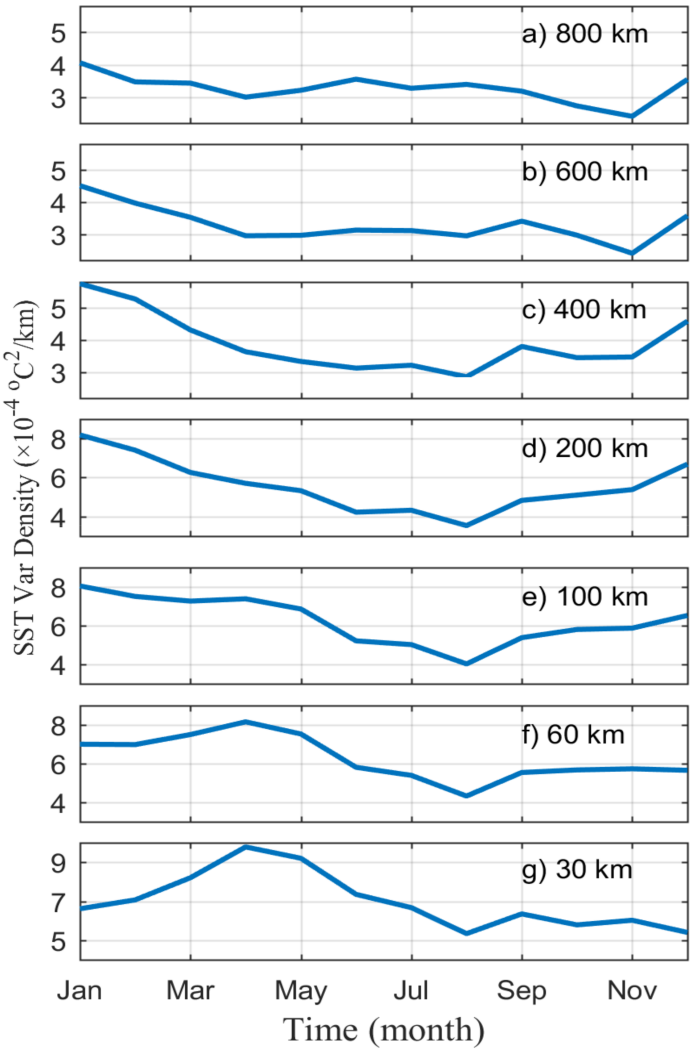

Figure 8. Seasonal variability of $V'(r)$ at different spatial scales during 2015.

As shown in Figures 7a and 8, the magnitude of $V'(r)$ highly depends on the spatial scale. Thus, in order to better compare the seasonal variability in the phase of the scale-dependent $V'(r)$, we calculated the normalized seasonal variability of $V'(r)$ for each scale. Figure 9 shows the scale–seasonal variability of the normalized $V'(r)$. One can see an obvious shift in the maximum $V'(r)$ from January at the large scale to April at the submesoscale, which implies the occurrence of forward energy cascade during this time period. The physical mechanism of the $V'(r)$ seasonal variability can be discussed through a budget analysis of SST spatial variance based on 4-D model data, which will be conducted in a future work.

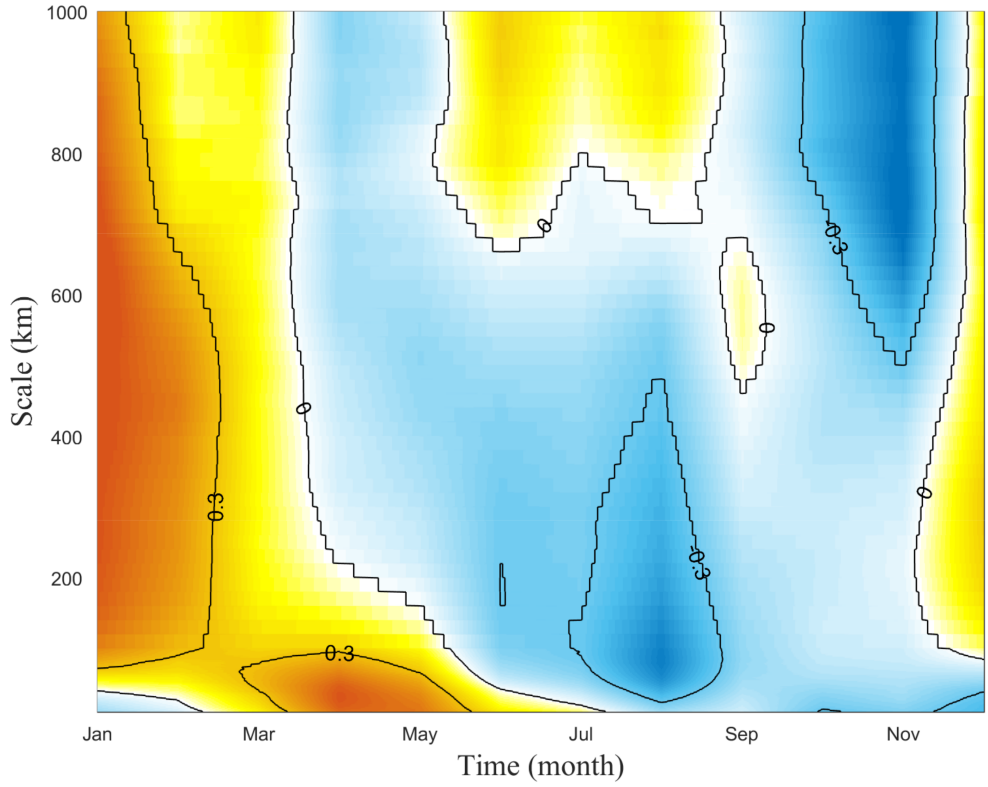

Figure 9. Scale–seasonal variability of normalized $V'(r)$ during 2015.

4.2.3. Latitudinal Variability

In this work, $V(r)$ is calculated from 1-D spatial series along the cross-track direction (close to the east–west direction), which allows us to obtain the latitudinal variability of $V(r)$ and $V'(r)$. As shown in Figure 10, the latitudinal variability of $V'(r)$ is independent of scales. $V'(r)$ is strongest around 41°N, which is consistent with the latitude of the strongest background SST front [30,31], and gradually decreases towards both sides. A second peak of the latitude-dependent $V'(r)$ is located around 36°N, which is consistent with the latitude of the strongest TKE, where the KE jet enters the North Pacific [26]. Another weaker peak occurs around 28°N, which belongs to the North Pacific subtropical countercurrent (STCC) region (between 20°N and 25°N). The result implies that the selected research region is beyond the KE region. However, the effects of the STCC on the SST spatial variance are limited in our study.

Figure 11 compares the correlation between the latitude-dependent $V'(r)$ at 600 km and the annual mean SST latitudinal gradient calculated by the GHRSST L4 product. They are highly correlated with a correlation coefficient of 0.96. The result demonstrates that the background SST front is the main source of SST spatial variance at any scale.

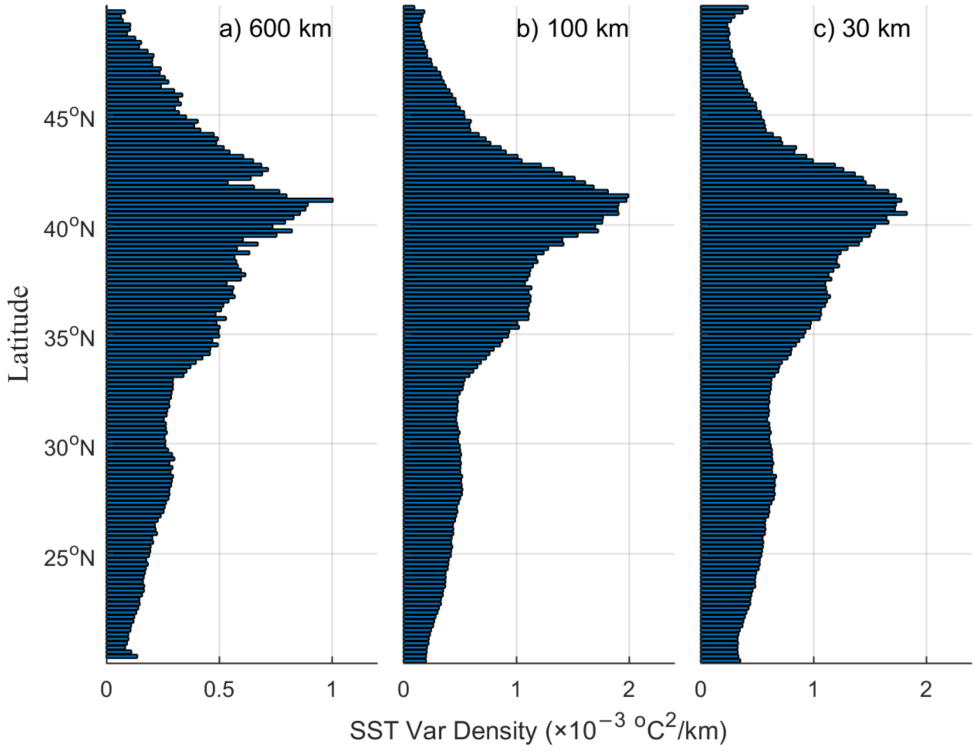

Figure 10. Latitude-dependent $V'(r)$ at (**a**) 600 km (large-scale), (**b**) 100 km (mesoscale), and (**c**) 30 km (submesoscale).

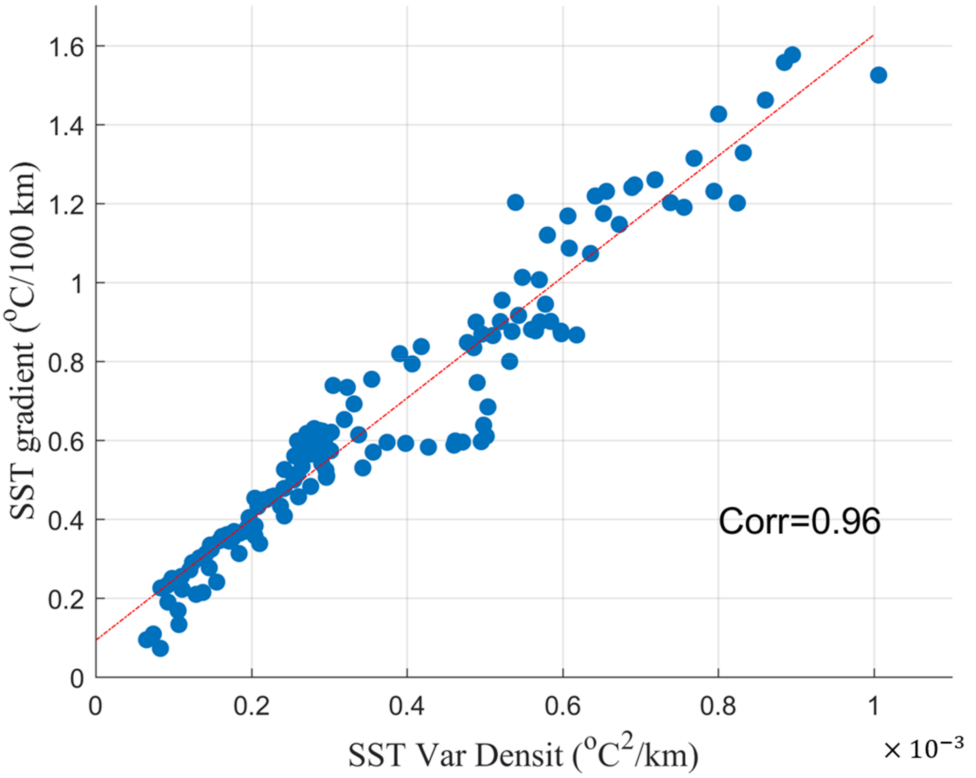

Figure 11. Scatter plots of $V'(r)$ at 600 km scale against annual mean SST latitudinal gradient. The red line represents the line of best fit.

5. Conclusions and Discussions

The abundant, but patchy L2P along-track high-resolution SST data are firstly used to reveal the statistical characteristics of the multiscale (1–1000 km) SST fractal structure with the second order structure function and spatial variance methods. The same power-law distribution with the slopes close to $r^{2/3}$ ($k^{-5/3}$) is found by different methods, which obeys the surface QG theory. In addition, the newly developed spatial variance method is superior in describing the multiscale fractal structure, compared with the traditional second order structure function by fBm experiments. Both two methods have high tolerance for missing points, and the former is proved to measure the accurate energy density and have a high utilization ratio of the data.

The slope of $V(r)$ shows obvious seasonal variability, and the variability at the large scale has an opposite seasonal cycle compared to the small scale (meso- and submesoscale) results. The $V'(r)$ is basically invariant at the scales larger than 400 km and gradually increases as the scale decreases. The submesoscale $V'(r)$ increases significantly, and is even three times larger than the results of other scales. The diurnal variability of $V'(r)$ is quite weak, with slightly higher values during daytime at the large scale. For the seasonal variability, the maximum $V'(r)$ usually occurs in winter and gradually switches to spring, which implies a forward energy cascade may occur during this time. Meanwhile, the minimum $V'(r)$ occurs in November at the scales larger than 600 km and in August at other scales. In addition to the seasonal variability, the latitude-dependent $V'(r)$ shows that the strongest SST spatial variance always occurs around 41°N at all spatial scales. There is a high relation, with a correlation coefficient of as high as 0.96, between the latitude-dependent $V'(r)$ and the background SST latitudinal gradient, which demonstrates that the background SST front is the basis of the occurrence of strong SST fluctuations over the KE region.

This work successfully reveals the statistical characteristics of the multiscale SST fractal structure from the VIIRS L2P satellite radiometer products. The direction of the energy transfer across different scales is still a question to be debated for the mesoscale in an atmospheric research field [32–37] and for the submesoscale in an oceanic research field [9,38,39]. This work provides observational evidence for this question. In order to further discuss interactions and energy cascade processes between different scales, a budget analysis is necessary based on a 4-D high-resolution model data, such as the LLC4320 simulated by the Massachusetts Institute of Technology general circulation model (MITgcm) on a latitude–longitude polar cap (LLC) grid [40,41]. This work is also expected to be extended to a longer time scale, such as the interannual variability, but it requires a huge amount of calculation. Meanwhile, this work is meaningful and useful for the application of other L2P satellite data products, such as the ocean color product, altimeter product, and the forthcoming Surface Water Ocean Topography (SWOT) satellite product, in future statistical research of the oceanic fractal structure.

Author Contributions: K.Y. and C.D. conceived and designed the experiments; K.Y. and Y.Y. performed the experiments; K.Y. and J.W. analyzed the data; K.Y. and J.W. wrote the paper. X.C. and Y.Y. helped modify the manuscript. All authors have read and agreed to the published version of the manuscript.

Funding: This work is supported by the National Key Research Program of China (2017YFA0604100), Fundamental Research Funds for the Central Universities (B220201024), the National Science Foundation of China (41606021), and the Open Fund of State Key Laboratory of Satellite Ocean Environment Dynamics, Second Institute of Oceanography (QNHX2120).

Data Availability Statement: The L2 VIIRS SST is supplied by GHRSST, and is available at https://www.ghrsst.org/ghrsst-data-services/services/ (accessed on 20 January 2018). The GHRSST L4 gridded SST data can be accessed from the Asia-Pacific Data-Research Center (APDRC) at http://apdrc.soest.hawaii.edu/datadoc/ghrsst_v1_ukmo.php (accessed on 24 January 2022).

Acknowledgments: The fractional Brownian motion data were generated using a MATLAB script written by Anders Holtsberg and available at http://se.mathworks.com/matlabcentral/newsreader/view_thread/16679 (accessed on 24 January 2018).

Conflicts of Interest: The authors declare that they have no known competing financial interests or personal relationships that could have appeared to influence the work reported in this paper.

References

1. Kolmogrov, A.N. The local structure of turbulence in incompressible viscous fluid for very large Reynolds numbers. *Dokl. Akad. Nauk SSSR.* **1941**, *30*, 299–303.
2. Kraichnan, R.H. Inertial ranges in two-dimensional turbulence. *Phys. Fluids.* **1967**, *10*, 1417–1423. [CrossRef]
3. Charney, J.G. Geostrophic turbulence. *J. Atmos. Sci.* **1971**, *28*, 1087–1095. [CrossRef]
4. Blumen, W. Uniform potential vorticity flow. Part I: Theory of wave interactions and two-dimensional turbulence. *J. Atmos. Sci.* **1978**, *35*, 774–783. [CrossRef]
5. Klein, P.; Treguier, A.M.; Hua, B.L. Three-dimensional stirring of thermohaline fronts. *J. Mar. Res.* **1998**, *56*, 589–612. [CrossRef]
6. Gage, K.S. Evidence for a k-5/3 law inertial range in mesoscale two-dimensional turbulence. *J. Atmos. Sci.* **1979**, *36*, 1950–1954. [CrossRef]
7. Nastrom, G.D.; Gage, K.S. A climatology of atmospheric wavenumber spectra of wind and temperature observed by commercial aircraft. *J. Atmos. Sci.* **1985**, *42*, 950–960. [CrossRef]
8. Lindborg, E. Can the atmospheric kinetic energy spectrum be explained by two-dimensional turbulence? *J. Fluid Mech.* **1999**, *388*, 259–288. [CrossRef]
9. Scott, R.B.; Wang, F. Direct evidence of an oceanic inverse kinetic energy cascade from satellite altimetry. *J. Phys. Oceanogr.* **2005**, *35*, 1650–1666. [CrossRef]
10. Callies, J.; Ferrari, R. Interpreting energy and tracer spectra of upper-ocean turbulence in the submesoscale range (1–200 km). *J. Phys. Oceanogr.* **2013**, *43*, 2456–2474. [CrossRef]
11. McCaffrey, K.; Fox-Kemper, B.; Forget, G. Estimates of ocean macroturbulence: Structure function and spectral slope from Argo profiling floats. *J. Phys. Oceanogr.* **2015**, *45*, 1773–1793. [CrossRef]
12. Cao, C.; DeLuccia, F.; Xiong, X.; Wolfe, R.; Weng, F. Early on- orbit performance of the Visible Infrared Imaging Radiometer Suite (VIIRS) onboard the Suomi National Polar-orbiting Partnership (S-NPP) satellite. *IEEE Trans. Geosci. Remote Sens.* **2013**, *52*, 1142–1156. [CrossRef]
13. Lee, E.L.; Miller, S.D.; Turk, F.J. The NPOESS VIIRS day/night visible sensor. *Bull. Am. Meteorol. Soc.* **2010**, *87*, 191–199. [CrossRef]
14. Capet, X.; McWilliams, J.C.; Molemaker, M.J.; Shchepetkin, A.F. Mesoscale to submesoscale transition in the California Current System. Part III: Energy balance and flux. *J. Phys. Oceanogr.* **2008**, *38*, 2256–2269. [CrossRef]
15. Qiu, B.; Chen, S.; Klein, S.P.; Sasaki, H.; Sasai, Y. Seasonal mesoscale and submesoscale eddy variability along the North Pacific Subtropical Countercurrent. *J. Phys. Oceanogr.* **2014**, *44*, 3079–3098. [CrossRef]
16. Callies, J.; Ferrari, R.; Klymak, J.; Gula, J. Seasonality in submesoscale turbulence. *Nat. Commun.* **2015**, *6*, 6862. [CrossRef]
17. Rocha, C.B.; Gille, S.T.; Chereskin, T.K.; Menemenlis, D. Seasonality of submesoscale dynamics in the Kuroshio Extension. *Geophys. Res. Lett.* **2016**, *43*, 11304–11311. [CrossRef]
18. Sasaki, H.; Klein, P.; Sasai, Y.; Qiu, B. Regionality and seasonality of submesoscale and mesoscale turbulence in the North Pacific Ocean. *Ocean Dynam.* **2017**, *67*, 1195–1216. [CrossRef]
19. Zhong, Y.; Bracco, A.; Tian, J.; Dong, J.; Zhao, W.; Zhang, Z. Observed and simulated submesoscale vertical pump of an anticyclonic eddy in the South China Sea. *Sci. Rep.* **2017**, *7*, 44011. [CrossRef]
20. Vogelzang, J.; King, G.P.; Stoffelen, A. Spatial variances of wind fields and their relation to second-order structure functions and spectra. *J. Geophys. Res. Oceans* **2015**, *120*, 1048–1064. [CrossRef]
21. Yu, K.; Dong, C.; King, G.P. Turbulent kinetic energy of the ocean winds over the Kuroshio Extension from QuikSCAT winds (1999–2009). *J. Geophys. Res. Oceans* **2017**, *122*, 4482–4499. [CrossRef]
22. Kelly, K.; Small, R.; Samelson, R.; Qiu, B.; Joyce, T.; Kwon, Y.; Cronin, M. Western boundary currents and frontal air-sea interaction: Gulf stream and Kuroshio extension. *J. Clim.* **2010**, *23*, 5644–5667. [CrossRef]
23. Booth, J.F.; Thompson, L.; Patoux, J.; Kelly, K.A.; Dickinson, S. The signature of the midlatitude tropospheric storm tracks in the surface winds. *J. Clim.* **2010**, *23*, 1160–1174. [CrossRef]
24. Wyrtki, K.; Magaard, L.; Hagar, J. Eddy energy in the oceans. *J. Geophys. Res. Oceans* **1976**, *81*, 2641–2646. [CrossRef]
25. Qiu, B. Variability and energetics of the Kuroshio Extension and its recirculation gyre from the first two-year TOPEX data. *J. Phys. Oceanogr.* **1995**, *25*, 1827–1842. [CrossRef]
26. Dong, J.; Fox-Kemper, B.; Zhang, H.; Dong, C. The seasonality of submesoscale energy production, content, and cascade. *Geophys. Res. Lett.* **2020**, *47*, e2020GL087388. [CrossRef]
27. Webb, E.K. Ratio of spectrum and structure-function constants in the inertial subrange. *Quart. J. Roy. Meteor. Soc.* **1964**, *90*, 344–345. [CrossRef]
28. Boyd, J.P. The energy spectrum of fronts: Time evolution of shocks in Burgers' equation. *J. Atmos. Sci.* **1992**, *49*, 128–139. [CrossRef]

29. Erickson, Z.K.; Thompson, A.F.; Callies, J.; Yu, X.; Garabato, A.N.; Klein, P. The vertical structure of open-ocean submesoscale variability during a full seasonal cycle. *J. Phys. Oceanogr.* **2020**, *50*, 145–160. [CrossRef]
30. Nonaka, M.; Nakamura, H.; Tanimoto, Y.; Kagimoto, T.; Sasaki, H. Decadal variability in the Kuroshio–Oyashio extension simulated in an eddy-resolving OGCM. *J. Clim.* **2006**, *19*, 1970–1989. [CrossRef]
31. Jing, Z.; Chang, P.; Shan, X.; Wang, S.; Wu, L.; Kurian, J. Mesoscale SST dynamics in the Kuroshio–Oyashio extension region. *J. Phys. Oceanogr.* **2019**, *49*, 1339–1352. [CrossRef]
32. VanZandt, T.E. A universal spectrum of buoyancy waves in the atmosphere. *Geophys. Res. Lett.* **1982**, *9*, 575–578. [CrossRef]
33. Lilly, D.K. Stratified turbulence and the mesoscale variability of the atmosphere. *J. Atmos. Sci.* **1983**, *40*, 749–761. [CrossRef]
34. Vallis, G.K.; Shutts, G.J.; Gray, M.E.B. Balanced mesoscale motion and stratified turbulence forced by convection. *Q. J. R. Meteorol. Soc.* **1997**, *123*, 1621–1652. [CrossRef]
35. Cho, J.Y.N.; Lindborg, E. Horizontal velocity structure functions in the upper troposphere and lower stratosphere: 1. Observations. *J. Geophys. Res.* **2001**, *106*, 10223–10232. [CrossRef]
36. Hamilton, K.; Takahashi, Y.O.; Ohfuchi, W. Mesoscale spectrum of atmospheric motions investigated in a very fine resolution global general circulation model. *J. Geophys. Res.* **2008**, *113*, D18110. [CrossRef]
37. Waite, M.L.; Snyder, C. Mesoscale energy spectra of moist baroclinic waves. *J. Atmos. Sci.* **2013**, *70*, 1242–1256. [CrossRef]
38. D'Asaro, E.; Lee, C.; Rainville, L.; Thomas, L. Enhanced turbulence and energy dissipation at ocean fronts. *Science* **2011**, *332*, 318–322. [CrossRef]
39. Zhang, Z.; Tian, J.; Qiu, B.; Zhao, W.; Chang, P.; Wu, D.; Wan, X. Observed 3D structure, generation, and dissipation of oceanic mesoscale eddies in the South China Sea. *Sci. Rep.* **2016**, *6*, 24349. [CrossRef]
40. Menemenlis, D.; Campin, J.; Heimbach, P.; Hill, C.; Lee, T.; Nguyen, A.; Schodlok, M.; Zhang, H. ECCO2: High resolution global ocean and sea ice data synthesis. *Mercator Ocean Quart. Newsl.* **2008**, *31*, 13–21.
41. Forget, G.; Campin, J.-M.; Heimbach, P.; Hill, C.N.; Ponte, R.M.; Wunsch, C. ECCO version 4: An integrated framework for non-linear inverse modeling and global ocean state estimation. *Geosci. Model Dev.* **2015**, *8*, 3653–3743. [CrossRef]

Disclaimer/Publisher's Note: The statements, opinions and data contained in all publications are solely those of the individual author(s) and contributor(s) and not of MDPI and/or the editor(s). MDPI and/or the editor(s) disclaim responsibility for any injury to people or property resulting from any ideas, methods, instructions or products referred to in the content.